Electronic materials

CrossMark

Controlling the morphology and size of (Gd$_{0.98-x}$Tb$_{0.02}$Eu$_x$)$_2$O$_3$ phosphors presenting tunable emission: formation process and luminescent properties

Wenzhi Wang[1] (ID), Jinkai Li[1,*] (ID), and Zongming Liu[1,*] (ID)

[1] *School of Materials Science and Engineering, University of Jinan, Jinan 250022, Shandong, China*

ABSTRACT

The (Gd$_{0.98-x}$Tb$_{0.02}$Eu$_x$)$_2$O$_3$ phosphors have been successfully obtained using the urea-based homogeneous precipitation method in the present work. The particle growth of the precursors with mono-dispersion spherical morphology is surface-diffusion controlled and precipitated in the order of the Tb(OH)CO$_3$ > Gd(OH)CO$_3$ > Eu(OH)CO$_3$, and the formation process has been also studied in detail. Partially replacing the pure water with ethylene glycol (EG) can control the particle size and morphology owing to its lower permittivity constant and interface energy. By monitoring the excitation at 314 nm ($4f^8 \rightarrow 4f^7 5d^1$ transition of Tb^{3+}), the (Gd$_{0.98-x}$Tb$_{0.02}$Eu$_x$)$_2$O$_3$ phosphors exhibit both Tb^{3+} (green) and Eu^{3+} (red) emissions at 547 and 613 nm, respectively. The presence of Gd^{3+} and Tb^{3+} excitation bands on the PLE spectra by monitoring the Eu^{3+} emission directly provides an evidence of the Tb$^{3+} \rightarrow$ Eu^{3+} and Gd$^{3+} \rightarrow$ Eu^{3+} energy transfer, respectively. The quenching concentration is determined to be 2.0 at.%, and the quenching mechanism is determined to be the exchange reaction between Eu^{3+}. The emission color can be readily tuned from approximately green to red via adjusting the Eu^{3+} content. The temperature-dependent analysis has been performed, and the results indicate that the (Gd$_{0.98-x}$Tb$_{0.02}$Eu$_x$)$_2$O$_3$ samples possess good thermal stability. Owing to the Tb$^{3+} \rightarrow$ Eu^{3+} energy transfer, the lifetime for the Tb^{3+} emission rapidly decreases, and the energy transfer efficiency has been calculated. The EG addition does not bring appreciable changes to the lifetime values for the both Tb^{3+} and Eu^{3+} emissions, but enhances remarkably the luminescent intensity which confirms the variation of the particle morphology/size, and the reason can be explained by the scattering of the light. The (Gd$_{0.98-x}$Tb$_{0.02}$Eu$_x$)$_2$O$_3$ phosphors developed in this work hopefully meet the requirements of various lighting and optical display applications.

Wenzhi Wang and Jinkai Li have contributed equally to this paper.

Address correspondence to E-mail: mse_lijk@ujn.edu.cn; ost_liuzm@ujn.edu.cn

Springer

Introduction

Rare-earth oxides (RE_2O_3, RE = rare-earth element) as the host materials have been studied widely by lots of researchers, including their synthesis and luminescent behaviors in the past few years. Owing to their unique physical and chemical properties [1–3], the rare-earth (RE) activated ions-doped RE_2O_3 oxide has been widely applied in the white LEDs, cathode-ray tubes (CRT), field-emission displays (FED), electroluminescent devices (ED), plasma display panels (PDP) and so on [4–6]. Among the rare-earth oxide RE_2O_3, the Gd_2O_3 might be the best known. The Gd_2O_3 with cubic-structured (space group: $Ia\bar{3}$) is the promising host material which is ascribed to its low photon energy and high refractive index [7, 8]. The Gd^{3+} in Gd_2O_3 systems can be easily replaced by the activated ions (such as Eu^{3+}, Tb^{3+}, Dy^{3+} and so on) and exhibit the colorful emission under the UV excitation. The Eu^{3+} and Tb^{3+} ions-activated Gd_2O_3 are the famous red and green-emitting phosphors, respectively, owing to their simple chemical composition, excellent luminescent efficiency, high color purity and so on [9–11].

The $(Gd_{0.98-x}Tb_{0.02}Eu_x)_2O_3$ systems have been chosen in this paper according to the following main reasons: (1) the luminescent properties of the phosphors heavily depend on the particle size and morphology [12–14] which in turn depend on the synthesis route used [15]. The phosphors with spheres, nanorods, nanowires, nanoplates, and flower plates morphologies have been widely prepared by various methods in recent years, such as the complexing-agent-assisted hydrothermal process [12], the homogeneous precipitation method [16], the carbonate precipitation [17] and so on. Until so far, the Gd_2O_3:Tb^{3+}/Eu^{3+} phosphors which are prepared by the urea-based homogeneous precipitation combined with the polyol method have not been widely studied yet. In addition, the ratio of ethylene glycol/deionized water (EG/DI) plays an important role in the morphology and luminescent property of the phosphors which has been demonstrated in the preparation of $(Y,Gd)_2O_3$:Eu^{3+} microsheet solution using the continue microwave irradiation [18, 19]. Based on these considerations, this work proposed a facile urea-based homogeneous precipitation combined with the polyol method to prepare the Gd_2O_3:Tb^{3+}/Eu^{3+} phosphors with different sizes as well as morphologies, and the morphology/size can be efficiently controlled by adjusting the ratio of EG/DI content; (2) the emission intensity can be improved via the energy transfer between the rare-earth ions. The Tb^{3+} ions have been frequently used as the sensitizer to enhance the Eu^{3+} emission in the $Gd_3Al_5O_{12}$:Tb/Eu [20], Y_2O_3:Tb/Eu [21], Lu_2O_3:Tb/Eu [22] phosphor systems and so on. Furthermore, the green emission of Tb^{3+} ($^5D_4 \rightarrow {}^7F_{1,2}$ transition of Tb^{3+}) and red emission of Eu^{3+} ($^5D_0 \rightarrow {}^7F_{1,2}$ transition of Eu^{3+}) can be sensitized by the efficient $Gd^{3+} \rightarrow Tb^{3+}$ and $Gd^{3+} \rightarrow Eu^{3+}$ energy transfers, respectively [23, 24]. It can be expected that the luminescent properties of Eu^{3+} and Tb^{3+} in Gd_2O_3 systems will be better than in the Y_2O_3 and Lu_2O_3 host matrices, which has been verified in the following experiments in this paper. Based on these, it can predict that the efficient $Gd^{3+} \rightarrow Tb^{3+}$, $Gd^{3+} \rightarrow Eu^{3+}$ and $Tb^{3+} \rightarrow Eu^{3+}$ energy transfers exist in $(Gd_{0.98-x}Tb_{0.02}Eu_x)_2O_3$ systems. It is reported that the part or whole energy of Tb^{3+} could be transferred to the Eu^{3+}, further enhances the red emission of Eu^{3+} [20], which can allow the emission color to be readily tuned through adjusting the Eu^{3+} concentration [25–28]; (3) the Gd^{3+} has more smaller electro-negativity (1.20) than that of the Y^{3+} (1.22) and the Lu^{3+} (1.27), which may result in an easier charge transfer (CT) and enhance the emission intensity [29, 30]; (4) the luminescent mechanism especially the thermal stability, activation energy and energy transfer mechanism rarely reported in previous works has been investigated in detail in the present work.

The $(Gd_{0.98}Tb_{0.02}Eu_{0.02})_2O_3$ samples with different morphologies and particle sizes have been successfully prepared by the urea-based homogeneous precipitation combined with the polyol method. The particle size and morphology can be effectively controlled by adjusting the ratios of EG/DI content, and the emission color has been known to be tuned though varying the content of Eu^{3+} [25–28]. The properties of precursors and resultant products have been systematically investigated using the combined techniques of XRD, XPS, ICP-OES, FE-SEM, HR-TEM, PLE/PL spectroscopy and fluorescence decay analysis. In the following sections, we report the synthesis, morphology evolution, precipitation kinetic, and the luminescent properties (PLE/PL, decay behavior, thermal stable, activation energy, etc.) of the Gd_2O_3:Tb^{3+}/Eu^{3+} phosphors.

Experimental section

Materials

The starting chemicals used in the present work mainly contain the Gd_2O_3, Tb_4O_7 and Eu_2O_3 (99.99% pure, Huizhou Ruier Rare Chemical Hi-Tech Co. Ltd., Huizhou, China), $HOCH_2CH_2OH$ (AR, Tianjin Kermel Chemical Reagent Co. Ltd., Tianjin, China), $CO(NH_2)_2 \cdot 12H_2O$ (AR, Sinopharm Chemical Reagent Co. Ltd., Shanghai, China), and HNO_3 (AR, Sinopharm Chemical Reagent Co. Ltd., Shanghai, China). All the chemicals were used as received without further purification.

Preparation procedure

The rare-earth nitrates $RE(NO_3)_3$ (RE = Gd, Tb and Eu) were obtained via dissolving the Gd_2O_3, Tb_4O_7 and Eu_2O_3 in the hot HNO_3. The mother salt solution was achieved though mixing the $RE(NO_3)_3$ solutions according to the formula of $(Gd_{0.98-x}Tb_{0.02}Eu_x)_2O_3$. Adding the $CO(NH_2)_2 \cdot 12H_2O$ and different solvent (pure DI water or mixed solution of DI water and EG) to the mother solution and the total volume were kept at 500 mL. The mixed solutions were firstly homogenized under stirring for 60 min at 25 °C and then heated to 90 ± 1 °C within 60 min. Keeping the temperature at 90 ± 1 °C for 2 h, the precipitations were collected by centrifugation, washed repeatedly with DI water and alcohol, and dried in the air at 80 °C for 12 h. The dried precursors were firstly calcined in the air at 600 °C for 4 h to produce oxides and then calcined at 1000 °C for 2 h in N_2/H_2 (80 vol% N_2) gas mixture. The total contents of Gd^{3+}, Tb^{3+} and Eu^{3+} all were 0.015 mol/L in each case. The EG volume content, expressed as $y = EG/(EG + DI)$ volume (y = 0, 0.1, 0.2, 0.3, 0.4, 0.5), was varied to reveal EG addition effect on the particle morphology and size.

Characterization

The phase evolution was measured by the powder X-ray diffraction (XRD) using nickel-filtered CuKα radiation in the 2θ range 10°–50° at a scan speed of 4.0° 2θ/min (Model D8 ADVANCE, BRUKER Co., Germany). The chemical states of the constituents were performed by using the X-ray photoelectron spectroscopy (XPS) with an MgK X-ray source,

energy of 1220 eV, and the operating voltage of at 10 kV (ESCALAB 250 XI, Thermo Scientific, America). The cation contents of the samples were revealed by ICP-OES analysis (Model SPS3520DD-UV, SII Technologies, Chiba, Japan) with a detection limit of 0.01 wt%, following standard procedures, and the average of three measurements was used to denote the content for each element. The morphologies of the synthesized precursors and oxides were performed by a field-emission scanning electron microscope (FE-SEM) with an acceleration voltage of 10 kV (QUANTA FEG 250, FEI Co., America). The micromechanism of phosphors was performed by HR-Transmission Electron Microscope (HR-TEM) with the 200 kV acceleration voltage (JEM-2100F, JEOL, Japan). The PLE/PL spectra of the $(Gd_{0.98-x-}Tb_{0.02}Eu_x)_2O_3$ samples were obtained by a Fluorescence Spectrophotometer (FP-6500, JASCO Co., Japan) at room temperature equipped with a Φ60-mm intergating sphere (ISF-513, JASCO, Tokyo, Japan), and the excitation source is the 150-W Xe-lamp.

Results and discussion

The morphologies of $(Gd_{0.98-x}Tb_{0.02}Eu_x)_2O_3$ (x = 0–0.05) precursors using pure water as the reaction solvent are shown in Fig. 1. It can be seen that all the precursors have the similar average particle size of $\sim$ 300 nm, regardless of different Eu^{3+} content; the samples exhibit good dispersion and spherical morphology. The reason may be that the reaction has the similar nucleation rate of precipitation process, which is ascribed to the concentrations of the urea and Tb^{3+} ions were fixed, and the concentrations of Gd and Eu varied little.

The formation of $(Gd_{0.98-x}Tb_{0.02}Eu_x)_2O_3$ solid solution depends on the nucleation/growth processes, and the precipitation occurs at a certain degree of supersaturation S, which is given by the following formula [31]:

$$S = a_A a_B / K_{sp} \tag{1}$$

where the a_A and the a_B are the activities of partially hydrolyzed cation ($[Ln(OH)_x(H_2O)_y]^{3-x}$, $x + y = 6$, Ln = Gd, Tb, Eu) and the CO_3^{2-}, respectively. The K_{sp} is the solubility product constant. Only when the S achieves to the critical supersaturation S^*, the nucleation/growth processes can start. As earlier
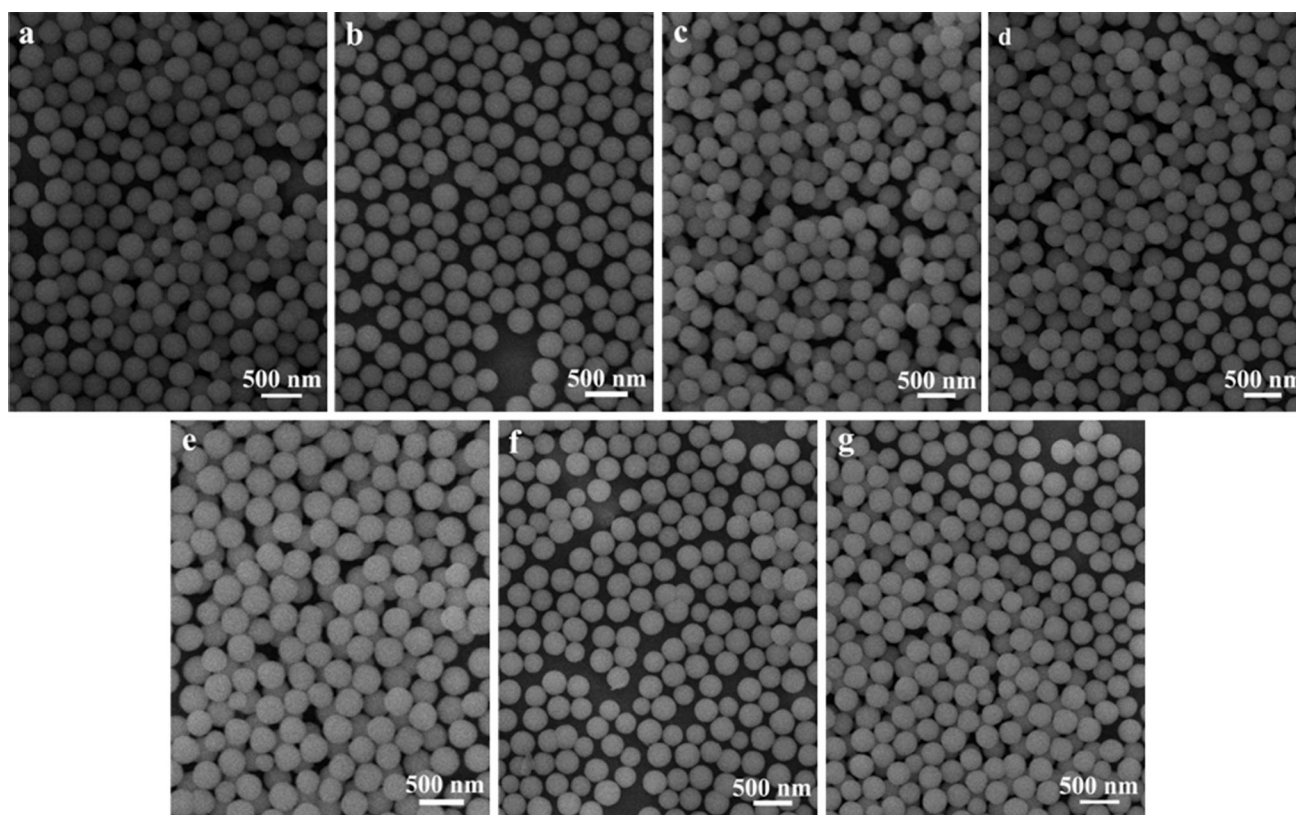
Figure 1 FE-SEM of $(Gd_{0.98-x}Tb_{0.02}Eu_x)_2O_3$ precursors with different Eu contents: **a** $x = 0$, **b** $x = 0.001$, **c** $x = 0.005$, **d** $x = 0.01$, **e** $x = 0.02$, **f** $x = 0.03$, **g** $x = 0.05$, respectively.

reports [32], the composition of the precursor synthesized via urea-based homogeneous precipitation has been determined to be lanthanide basic carbonate $Ln(OH)CO_3 \cdot nH_2O$. The solubility of lanthanide basic carbonate in the water increases with the ionic radius of Ln^{3+} ions decreasing. According to the lanthanide contraction law, it can be known that the value of K_{sp} increases according to priority of the $Tb(OH)CO_3 > Gd(OH)CO_3 > Eu(OH)CO_3$. Thus, the complexity of stable nuclei of $Ln(OH)CO_3$ formation increases in the same order. The homogeneous nucleation of $Eu(OH)CO_3$ starts in priority, and then the precipitations of the $Tb(OH)CO_3$ and $Gd(OH)CO_3$ occur on the already formed $Eu(OH)CO_3$ nuclei through heterogeneous nucleation.

In order to better understand the precipitation mechanism, we have regularly sampled and analyzed the particles formed in the different reaction stages, using the $(Gd_{0.96}Tb_{0.02}Eu_{0.02})_2O_3$ sample as an example. Figure 2 shows the FE-SEM morphologies of the precipitation at the different reaction times. From which it can be seen that the colloidal particles grow quite uniformly with the reaction time, which

indicates that the mixed systems can follow the LaMer model [33]. The growth rate of the nanoparticles can be consistent with the cubic-root law which is given the following formula:

$$D(t) = \sqrt[3]{Kt} \qquad (2)$$

where the $D(t)$ is the average particle diameter at the time of t, *in* which the t is reaction time, and the K is the growth rate. Figure S1 (Supporting Information Figure S1) shows the relationship between particle size $D(t)$ and the reaction time t, and the inset in Fig. S1 (in the Supporting Information) is the relationship particle size $D^3(t)$ and the reaction time t. From which it can be seen that the relationship between $D(t)^3$ and t presents good relationship which confirms with formula (2), indicating that the particle growth is surface-diffusion controlled even for the complicated Gd/Tb/Eu ternary system.

Figure 3a shows the XRD patterns of the $(Gd_{0.98-x}Tb_{0.02}Eu_x)_2O_3$ samples calcined at the same temperature of 1000 °C for 4 h. As shown in Fig. 3a, the Tb^{3+} and Eu^{3+} ions additions do not alter the crystal structure, and all the $(Gd_{0.98-x}Tb_{0.02}Eu_x)_2O_3$

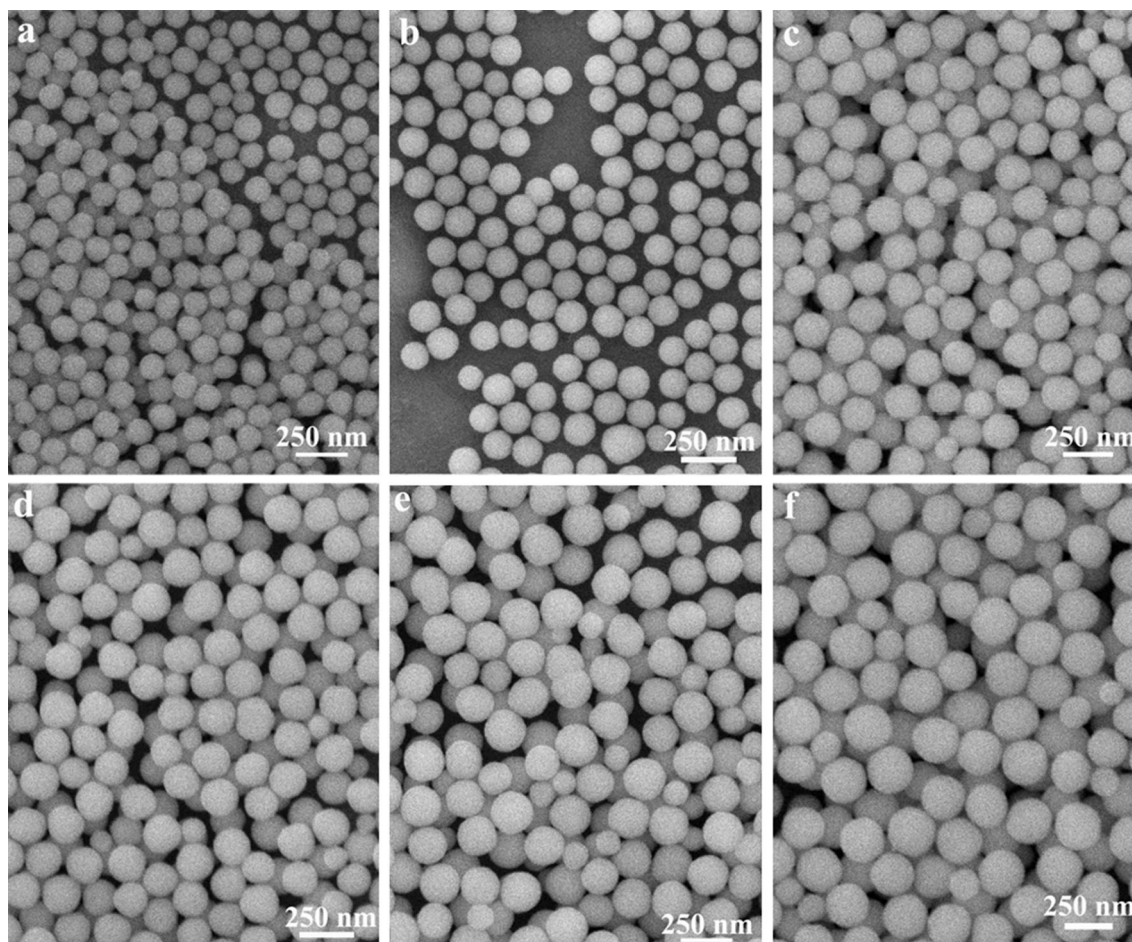**Figure 2** Time-course evolution of particle size for $(Gd_{0.96}Tb_{0.02}Eu_{0.02})_2O_3$ precursor, growth time: **a** 20 min, **b** 20 min, **c** 60 min, **d** 80 min, **e** 100 min, **f** 120 min, respectively.

samples can be well indexed to the Gd_2O_3 with cubic structure (space group: $Ia\bar{3}$(206), JCPDS No. 43-1014) [2], which indicates that the pure phase $(Gd_{0.98-x-}Tb_{0.02}Eu_x)_2O_3$ can be formed at 1000 °C. The main peak (222) is zoomed in Fig. 3b. It can be seen that the positions of main peak drift to the lower angle with the Eu^{3+} content increasing due to the lager ionic radius of Eu^{3+} (0.1066 nm) than that of Gd^{3+} (0.1053 nm) and Tb (0.1040 nm) [34]. Fixed at the same Tb^{3+} content of 2 at.%, Fig. 3c shows the calculated lattice constants of the $(Gd_{0.98-x}Tb_{0.02}Eu_x)_2O_3$ samples as a function of the Eu^{3+} content. Clearly, the cell parameter linearly increases with Eu^{3+} concentration increasing and follows Vegard's law, indicating that the homogeneous solid solutions have already been formed.

Figure 3d shows the typical XPS survey scan of the $(Gd_{0.96}Tb_{0.02}Eu_{0.02})_2O_3$ samples. As shown in Fig. 3d, the Gd, Tb, Eu, O and C exist in the XPS survey

spectra, indicating that the Tb^{3+} and Eu^{3+} ions have effectively been introduced into the Gd_2O_3 matrix materials. The XPS band of C1s was due to the adsorbed impurity carbon [35]. As shown in Fig. 3e, the two O1s XPS bands of samples are found at the 532.7 and 530.3 eV BE positions, owing to the O^{2-} of $(Gd_{0.96}Tb_{0.02}Eu_{0.02})_2O_3$ and the surface oxygen vacancies [35, 36]. The Gd 4d and Tb 4d were observed at the bands of 148.5 and 143.1 eV, respectively, which is shown in Fig. 3f. The positions of bands are consistent with the energy level for Gd and Tb in Gd_2O_3 and Tb_2O_3, respectively [37]. Thus, the valence states of the elements in the sample can be verified. Further observation is that only the Tb^{3+} ions is found at 148.5 eV in the 4d core-level spectrum of $(Gd_{0.96}Tb_{0.02}Eu_{0.02})_2O_3$ sample, which indicates that the Tb^{4+} was almost completely reduced to the Tb^{3+} [38]. Figure 3g shows the high XPS resolution Eu 3d spectra of the $(Gd_{0.96}Tb_{0.02}Eu_{0.02})_2O_3$

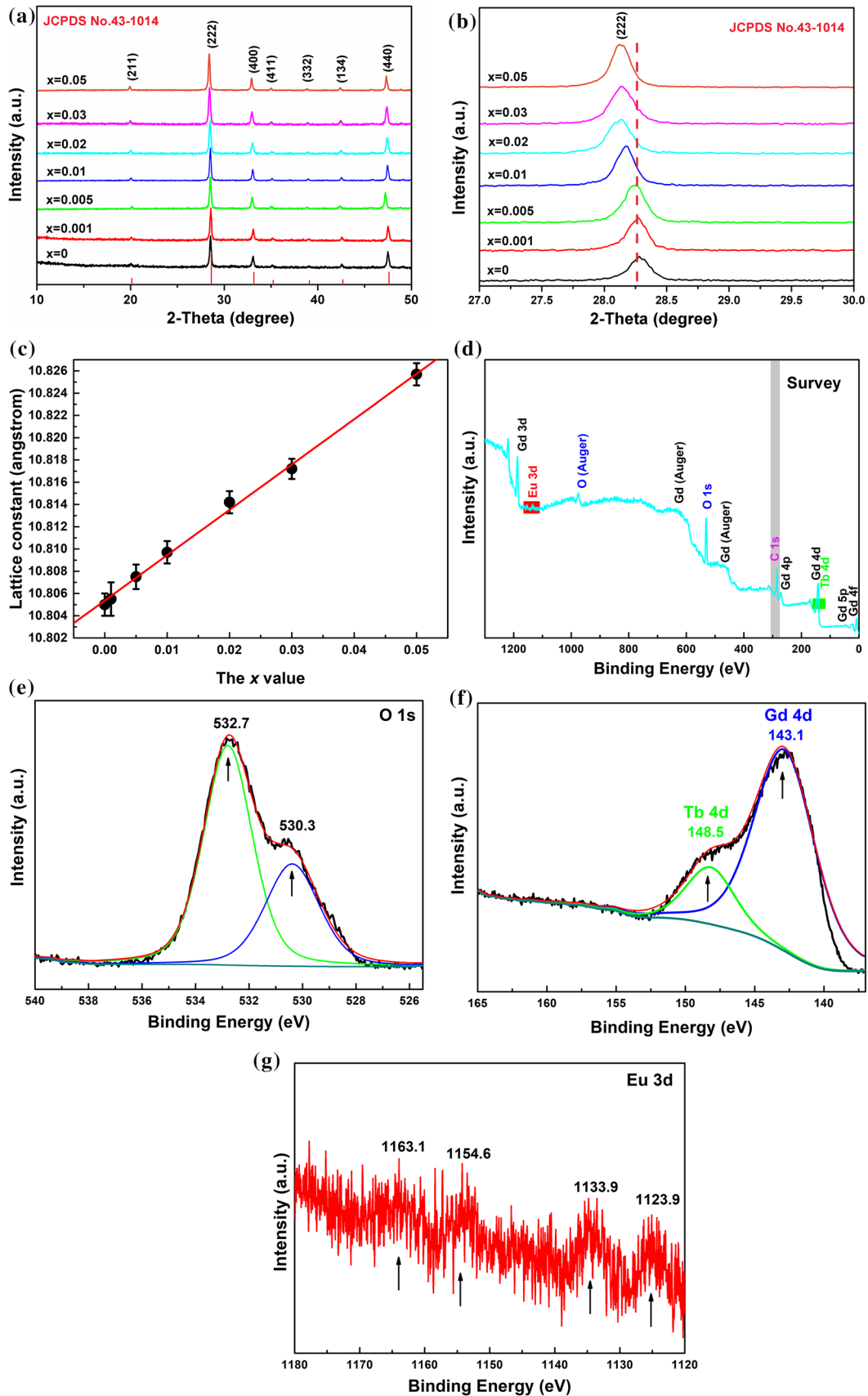◀**Figure 3** **a** XRD patterns of $(Gd_{0.98-x}Tb_{0.02}Eu_x)_2O_3$ precursors with different Eu contents (*x* value, *x* = 0–0.05). **b** The amplification diagram of main peak (222). **c** The lattice constants of the $(Gd_{0.98-x}Tb_{0.02}Eu_x)_2O_3$ oxides as a function of the Eu^{3+} content. **d** The XPS survey scan of $(Gd_{0.96}Tb_{0.02}Eu_{0.02})_2O_3$ oxides. **e**–**g** Are the high-resolution O1*s*, Gd 4d/Tb 4d and Eu 3d XPS spectra of $(Gd_{0.96}Tb_{0.02}Eu_{0.02})_2O_3$ oxides, respectively.

sample; the major bands of Eu 3d are found at 1123.9, 1133.9, 1154.6 and 1163.1 eV, respectively. The positions of energy bands are associated with the Eu^{3+} in Eu_2O_3 system [39].

The cation contents of the $(Gd_{0.98-x}Tb_{0.02}Eu_x)_2O_3$ phosphors obtained by the ICP-OES analysis are shown in Table 1. As shown in Table 1, the analyzed contents of samples are consistent with the values which were calculated from the prescribed chemical formula. The results indicate that the urea-based homogeneous precipitation method used in this work is very suitable to prepare rare-earth oxide phosphors with controllable chemical composition.

Figures S2a–S2g (Supporting Information Figure S2) show the FE-SEM of $(Gd_{0.98-x}Tb_{0.02}Eu_x)_2O_3$ precursors calcined at 1000 °C using pure water. As can be seen that the resultant products still keep the good dispersions and the spherical morphologies of precursors even calcined at 1000 °C. The reason for this phenomenon is that the negligible aggregations of spherical precursors make the contact areas between particles very limited [30, 40]. Figures S2h and S2i (in the Supporting Information) show the selected area electron diffraction (SAED) pattern and high-resolution (HR) TEM image of $(Gd_{0.96}Tb_{0.02}Eu_{0.02})_2O_3$ phosphors, respectively. As shown in Fig. S2h (in the Supporting Information), the results indicate that the $(Gd_{0.96}Tb_{0.02}Eu_{0.02})_2O_3$ samples

possess the highly single crystalline nature of the nanostructures. Further observation is that the interplanar distance (*d*) of the $(Gd_{0.96}Tb_{0.02}Eu_{0.02})_2O_3$ samples is ~ 0.274 nm (Supporting Information Figure S2i), which is consistent with the results of Gd_2O_3 in the database ($d_{(400)}$ = 0.270 nm, JCPDS No. 43-1014).

The PLE properties of the $(Gd_{0.98-x}Tb_{0.02}Eu_x)_2O_3$ phosphors using pure water as reaction solvent are displayed in Fig. 4. By monitoring the Tb^{3+} emission at 547 nm (the $^5D_4 \rightarrow {}^7F_5$ transition of Tb^{3+}, Fig. 4a), all the PLE spectra mainly contain three groups of excitation bands at ~ 223, ~ 276 and ~ 314 nm, respectively, which are arising from the $4f^8 \rightarrow 4f^75d^1$ transition of Tb^{3+}. Further observation is that the weak intensity peak ($^7F_6 \rightarrow {}^5L_{10-7}$ and $^7F_6 \rightarrow {}^5D_3$ intra-$4f^8$ transitions of Tb^{3+}) appears at ~ 375 nm (Fig. 4a). It can be clearly seen that the excitation bands intensities vary remarkably and decrease steadily with the Eu^{3+} contents increasing. By monitoring the Eu^{3+} emission at 613 nm (the $^5D_0 \rightarrow {}^7F_2$ transition of Eu^{3+}, Fig. 4b), besides the charge transfer (CTB, ~ 243 nm), $^7F_{0,1} \rightarrow {}^5L_7$ (~ 380 nm) and $^7F_{0,1} \rightarrow {}^5L_6$ (~ 394 nm) transitions of Eu^{3+}, the $4f^8 \rightarrow 4f^75d^1$ transitions of Tb^{3+} also appear at ~ 275 and ~ 314 nm in the PLE spectra, confirming the highly efficient energy transfer from Tb^{3+} to Eu^{3+}. It should be noted that the excitation peaks at ~ 275 and 314 nm overlap the characteristic transition $^8S_{7/2} \rightarrow {}^6I_J$ of Gd^{3+}, providing an evidence of the energy transfer from Gd^{3+} to Tb^{3+} and Eu^{3+}, respectively.

From above analysis, the exciting $(Gd_{0.98-x}Tb_{0.02}Eu_x)_2O_3$ phosphors at 314 nm can efficiently achieve the Tb^{3+} and Eu^{3+} emissions. Further observation is that the excitation peaks of $(Y_{0.96}Tb_{0.2}Eu_{0.2})_2O_3$ (at ~ 305 nm) and $(Lu_{0.96}Tb_{0.2}Eu_{0.2})_2O_3$ (at ~ 303 nm)

Table 1 Calculated and analyzed cation contents for nine typical phosphors

| Intended formula	Contents calculated/analyzed for cations (wt%)				
	Gd	Y	Lu	Tb	Eu
$(Gd_{0.98}Tb_{0.02})_2O_3$	85.01/84.46	–	–	1.75/1.75	–
$(Gd_{0.979}Tb_{0.02}Eu_{0.001})_2O_3$	84.92/85.13	–	–	1.75/1.81	0.08/0.10
$(Gd_{0.975}Tb_{0.02}Eu_{0.005})_2O_3$	84.59/84.97	–	–	1.75/1.76	0.42/0.46
$(Gd_{0.97}Tb_{0.02}Eu_{0.01})_2O_3$	83.17/83.01	–	–	1.75/1.79	0.84/0.89
$(Gd_{0.96}Tb_{0.02}Eu_{0.02})_2O_3$	83.32/83.24	–	–	1.75/1.75	1.68/1.69
$(Gd_{0.95}Tb_{0.02}Eu_{0.03})_2O_3$	82.48/83.05	–	–	1.75/1.78	2.52/2.45
$(Gd_{0.93}Tb_{0.02}Eu_{0.05})_2O_3$	80.79/81.28	–	–	1.75/1.80	4.20/4.14
$(Y_{0.96}Tb_{0.02}Eu_{0.02})_2O_3$	–	73.85/74.02	–	2.75/2.87	2.63/2.85
$(Lu_{0.96}Tb_{0.02}Eu_{0.02})_2O_3$	–	–	84.75/84.88	1.60/1.59	1.53/1.51
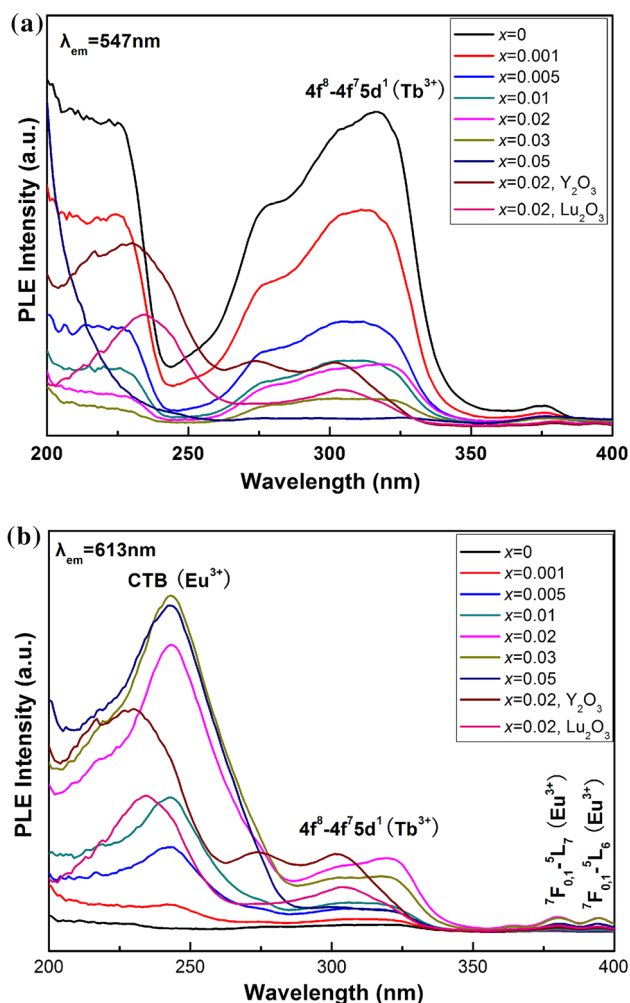
Figure 4 A comparison of the PLE behaviors of the $(Y_{0.96}Tb_{0.02}Eu_{0.02})_2O_3$, $(Lu_{0.96}Tb_{0.02}Eu_{0.02})_2O_3$ and $(Gd_{0.98-x}Tb_{0.02}Eu_x)_2O_3$ phosphors, the PLE spectra were obtained by monitoring the 547 nm (**a**) and 613 nm (**b**) emissions, respectively.

show gradually blueshift, but the excitation peaks of $(Y_{0.96}Tb_{0.2}Eu_{0.2})_2O_3$ (at $\sim$ 231 nm) and $(Lu_{0.96}Tb_{0.2}Eu_{0.2})_2O_3$ (at $\sim$ 235 nm) show gradually redshift on the PLE spectra compared to the $(Gd_{0.98-x}Tb_{0.02}Eu_x)_2O_3$ phosphors. This is mainly due to the lower electro-negativity of Gd^{3+} (1.20) than that of Y^{3+} (1.22) and Lu^{3+} (1.27). The lower electro-negativity would enhance the crystal field splitting of the 5d energy level, which can shift the low energy excitation peaks to the long wavelengths, and high energy excitation peaks to the short wavelength [24].

Figure 5 shows the photoluminescence properties of the $(Gd_{0.98-x}Tb_{0.02}Eu_x)_2O_3$ phosphors under 314 nm wavelength excitation with Eu^{3+} content changing, and the PL spectra of $(Y_{0.96}Tb_{0.02}Eu_{0.02})_2O_3$ and $(Lu_{0.96}Tb_{0.02}Eu_{0.02})_2O_3$ samples are also included for

the comparison. The $(Gd_{0.98}Tb_{0.02})_2O_3$ ($x = 0$) phosphor exhibits four groups of typical Tb^{3+} emission bands at $\sim$ 490 nm (blue), 547 nm (green, the strongest), 595 nm (orange-red) and 623 nm (red) which are associated with the $^5D_4 \rightarrow {}^7F_J$ ($J = 3, 4, 5, 6$) transitions of Tb^{3+} which are marked in Fig. 5a, respectively. However, the Tb^{3+}/Eu^{3+} co-doped samples not only contain the typical Tb^{3+} emission bands, but also the typical Eu^{3+} emission bands at $\sim$ 595, 613 nm (the strongest), 655 and 708 nm attributing to the $^5D_0 \rightarrow {}^7F_J$ ($J = 1, 2, 3, 4$) transitions of Eu^{3+}, respectively. There are two aspects which should be noted: (1) the intensities of blue emissions (< 480 nm) derived from the $^5D_3 \rightarrow {}^7F_J$ transitions of Tb^{3+} ($J = 3, 4, 5, 6$) are too weak to be detectable. The phenomena can be explained as follows: the spectral energy distribution of Tb^{3+} emission is strongly dependent on the Tb^{3+} concentrations. As the Tb incorporation increasing, the intensity of $^5D_3$ emission steadily decreased while the $^5D_4$ emission increased due to the cross-relaxation from $^5D_3$ to $^5D_4$ level. Owing to the high Tb^{3+} concentrations used in the present work, the $^5D_3$ emission is almost completely quenched; (2) the strongest emission of Eu^{3+} appears at $\sim$ 613 nm for the $^5D_0 \rightarrow {}^7F_2$ transition rather than $\sim$ 595 nm for the $^5D_0 \rightarrow {}^7F_1$ transition in the Tb^{3+}/Eu^{3+} co-doped samples. The mainly reason is that the occupancy of Eu^{3+} at C_2 sites without inversion symmetry (75%) is higher than the S_6 sites (25%) with inversion symmetry [41, 42].

Figure 5b shows the relative intensities of the 547 and 613 nm emissions as well as the I_{613}/I_{547} intensity ratios under 314 nm excitation. The emission intensities of Eu^{3+} increased with the Eu^{3+} content increasing up to 2 at.% ($x = 0.02$), and then decreased due to the concentration quenching. At the maximum Eu^{3+} emission intensity, the total activator concentration C_{Tb+Eu} of 4 at.% is close to the 5 at.% which had been widely reported in Gd_2O_3 system doped with either Eu^{3+} or Tb^{3+}. The interaction type of luminescence quenching for solid phosphors can be concluded via analyzing the constant s according to the following formula [34, 43]:

$$\log(I/c) = (-s/d)\log c + \log f \qquad (3)$$

where the I is the emission intensity, the c is the activator concentration, the d is the sample dimension ($d = 3$ for regular sample), the f is a constant, and the s is the index of electric multipole. The s values of 6, 8, and 10 represent the dipole–dipole, dipole–quadrupole, and quadrupole–quadrupole electric interactions, respectively,
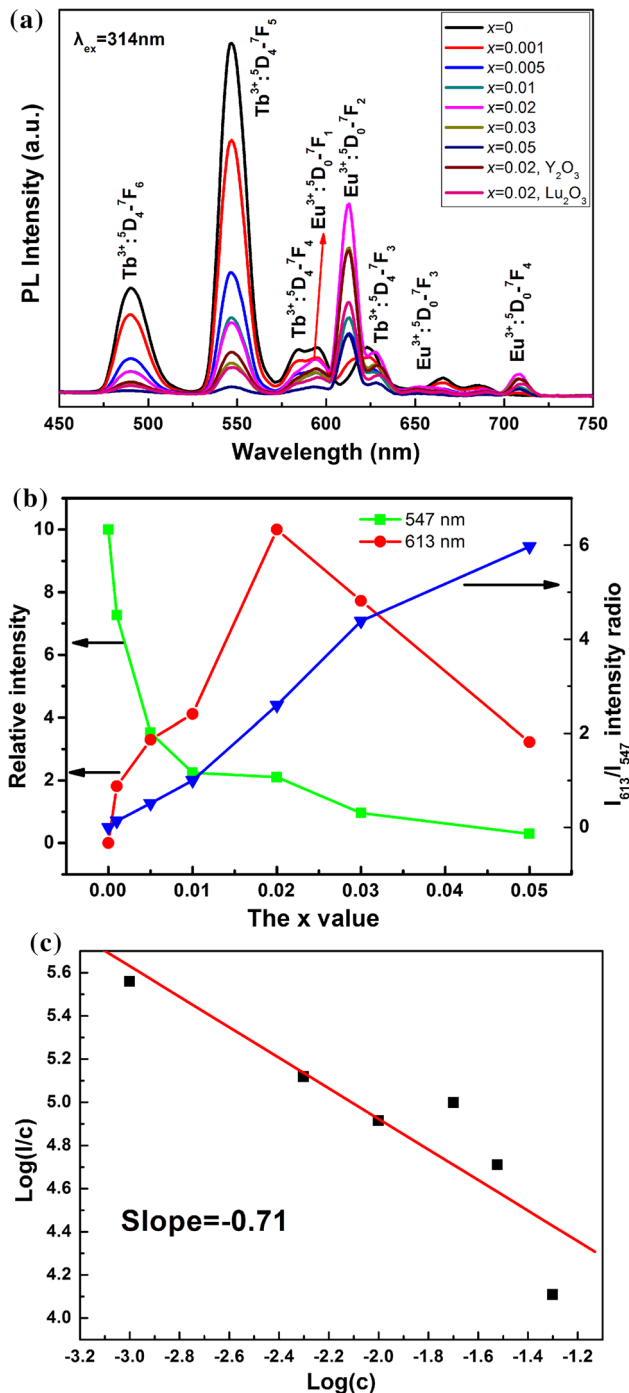
Figure 5 **a** Emission spectra of the $(Y_{0.96}Tb_{0.02}Eu_{0.02})_2O_3$, $(Lu_{0.96}Tb_{0.02}Eu_{0.02})_2O_3$ and $(Gd_{0.98-x}Tb_{0.02}Eu_x)_2O_3$ phosphors under 314 nm excitation and **b** presents relative intensities of the 547 nm emission of Tb^{3+} and the 613 nm emission of Eu^{3+} as well as the I_{613}/I_{547} intensity ratio, as a function of the Eu content (the x value). **c** Is the relationship between $\log(I/c)$ and $\log(c)$ of the $(Gd_{0.98-x}Tb_{0.02}Eu_x)_2O_3$ phosphors for Eu^{3+} emission.

whereas $s = 3$ corresponds to the exchange interaction. The relationship between $\log(I/c)$ and $\log(c)$ for 613 nm emission is shown in Fig. 5c. The slope $(-s/3)$ is determined to be -0.71 yielding the s value of the $(Gd_{0.98-x}Tb_{0.02}Eu_x)_2O_3$ samples is ~ 2.13, indicating that the concentration quenching is mainly due to the energy transfer between Eu^{3+} and Eu^{3+} [44, 45]. The Tb^{3+} emission intensity gradually decreased with the Eu^{3+} contention increasing while the I_{613}/I_{547} intensity ratio increased, which can provide the strong evidence of the highly efficient energy transfer from Tb^{3+} to Eu^{3+}. The luminescent intensity (regardless of Tb^{3+} or Eu^{3+} emission) of the $(Gd_{0.96}Tb_{0.02}Eu_{0.02})_2O_3$ was higher than that of the $(Y_{0.96}Tb_{0.02}Eu_{0.02})_2O_3$ and $(Lu_{0.96}Tb_{0.02}Eu_{0.02})_2O_3$ samples, which can provide an directly evidence of the $Gd^{3+} \rightarrow Tb^{3+}$ and the $Gd^{3+} \rightarrow Eu^{3+}$ energy transfers, respectively.

To further explain the energy transfer from Tb^{3+} to Eu^{3+}, the decay kinetics of Tb^{3+} ($^5D_4 \rightarrow {}^7F_5$ transition) and Eu^{3+} ($^5D_0 \rightarrow {}^7F_2$ transition) have been investigated ($\lambda_{ex} = 314$ nm), and then the lifetimes (τ_R) and the energy transfer efficiencies (η) of the phosphors can be calculated. The fluorescence decay curves of Tb^{3+} and Eu^{3+} emissions can be fitted with single exponential decay in the following formula:
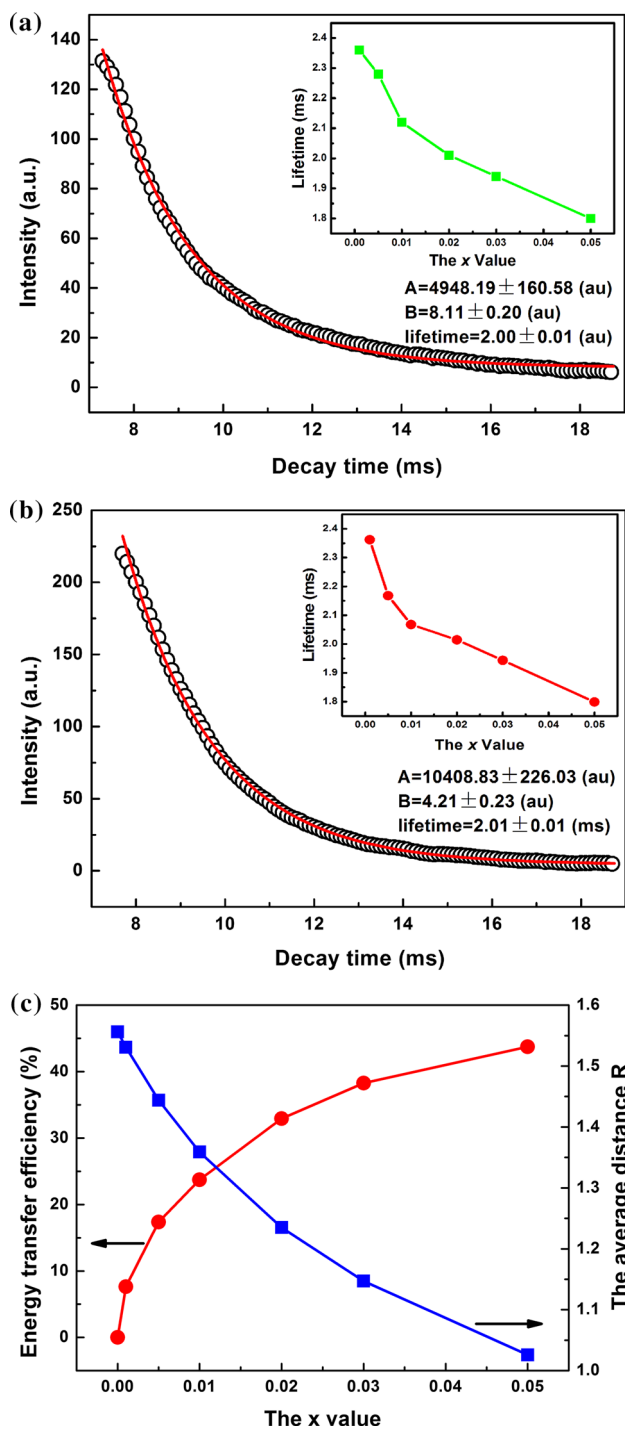
$$I = A \exp(-t/\tau_R) + B \tag{4}$$

where the τ_R is fluorescence lifetime, the t is decay time, the I is the relative fluorescence intensity, and A and B are the constants. It can be seen that the lifetime values of the Tb^{3+} emission (the inset of Fig. 6a) decreased from ~ 2.98 to ~ 1.67 ms with the Eu^{3+} content (the x value) increasing from $x = 0$ to $x = 0.05$, attributing to the efficient $Tb^{3+} \rightarrow Eu^{3+}$ energy transfer. Meanwhile, the lifetime values of the Eu^{3+} emission slowly and continuously decrease at the higher concentration of Eu^{3+} (the inset of Fig. 6b). The higher Eu^{3+} concentration will lead to the formation of a resonant energy transfer network between the activators, which can act as an additional channel to the non-radiative centers of particle surface and therefore shorten the lifetime.

The energy transfer efficiency (η) of $Tb^{3+} \rightarrow Eu^{3+}$ can be calculated by the following formula:

$$\eta = 1 - \frac{\tau}{\tau_0} \tag{5}$$

where the τ and the τ_0 are the lifetimes of Tb^{3+} in the presence and absence of Eu^{3+}, respectively. The results of calculation are shown in Fig. 6c. It can be

◀**Figure 6** Fluorescence decay curves for the 547 nm (**a**) and 613 nm (**b**) emission of $(Gd_{0.96}Tb_{0.02}Eu_{0.02})_2O_3$ phosphors. The embedded graphs **a** and **b** are the fluorescence lifetime of the 547 and 613 nm for the $(Gd_{0.98-x}Tb_{0.02}Eu_x)_2O_3$ phosphors as a function of the Eu^{3+} content, respectively. **c** Energy transfer efficiency and average separation distance (R) of the activators, as a function of the Eu^{3+} content (the x value). The insets in graph **a** and **b** are the lifetimes of the 547 and 613 nm emissions for the $(Gd_{0.98-x}Tb_{0.02}Eu_x)_2O_3$ phosphors as a function of the Eu^{3+} contents.

energy transfer have been calculated theoretically. The mode of energy transfer (exchange interaction and multipolar interaction) depends on the average separation distance R between the donor and acceptor. The average separation distances for Tb^{3+} and Eu^{3+} in $(Gd_{0.98-x}Tb_{0.02}Eu_x)_2O_3$ phosphors can be calculated via the Blasse formula [46]:

$$R = 2\left(\frac{3V}{4\pi C_{Tb+Eu}N}\right)^{1/3} \tag{6}$$

where the C_{Tb+Eu} is the total concentrations of Tb^{3+} and Eu^{3+}, the V is the volume of unit cell, and the N is the number of available sites for the dopant per unit cell. The per unit cell of Gd_2O_3 sample has 80 atoms, among which 32 are the Ln^{3+} and thus the $N = 32$. The value of the V can be obtained from the lattice constant which is shown in Fig. S2c (in the Supporting Information). The R values of calculation are shown in Fig. 6c, as a function of Eu^{3+} content (the x value), showing that all the R values are significantly larger than the 0.3–0.4 nm. It indicates that the mode of $Tb^{3+} \rightarrow Eu^{3+}$ energy transfer is the electric multipolar interactions in the present work.

According to the early reported energy transfer process theory which is suggested by Dexter and Reisfeld [46–49], the types of interaction of electric multipole interactions can be analyzed by the following formula:

$$\frac{\eta_0}{\eta} \propto C^{n/3} \tag{7}$$

where the C is the total concentrations of Tb^{3+} and Eu^{3+} which could be replaced by the Eu^{3+} content owing to the fixed Tb^{3+} content, the η_0 and η are the luminescence quantum efficiencies of the Tb^{3+} in the absence and presence of Eu^{3+}, respectively. Meanwhile, the η_0/η ratio can be replaced by the PL intensity ratio I_{S0}/I_S. The $(I_{S0}/I_S) \propto C^{n/3}$ with n = 6, 8 and 10 corresponds to dipole–dipole, dipole–

seen that the $Tb^{3+} \rightarrow Eu^{3+}$ energy transfer efficiency increases from 7.62 to 43.74% with the Eu^{3+} content (the x value) increasing from $x = 0.001$ to $x = 0.05$, respectively.

In order to further elaborate the $Tb^{3+} \rightarrow Eu^{3+}$ energy transfer mechanism, the mode and type of the

quadrupole, and quadrupole–quadrupole interactions, respectively. The relationships between (I_{S0}/I_S) and $C^{n/3}$ are shown in Fig. S3 (Supporting Information Figure S3), from which it can be seen that the linear relationship with $n = 6$ (Supporting Information Figure S3a) was the best through the comparison of fitting factor values (R^2). The results indicate that the $Tb^{3+} \rightarrow Eu^{3+}$ energy transfer mechanism of the $(Gd_{0.98-x}Tb_{0.02}Eu_x)_2O_3$ samples is dominantly electric dipole–dipole interactions, as well as the critical distance (R_c) of energy transfer can be also proved.

The above analysis indicates that the multi-channel energy transfers may exist in the $(Gd_{0.98-x}Tb_{0.02}Eu_x)_2O_3$ phosphors which is shown in Fig. 7, such as $Gd^{3+} \rightarrow Eu^{3+}$, $Gd^{3+} \rightarrow Tb^{3+}$, $Tb^{3+} \rightarrow Eu^{3+}$ and $Gd^{3+} \rightarrow Tb^{3+} \rightarrow Eu^{3+}$. By monitoring the 314 nm excitation wavelength, the electrons of the $^8S_{7/2}$ ground state though absorbing the energy can transmit to the ^6P_J excited state of Gd^{3+}, meanwhile the $4f^8$ electrons of Tb^{3+} transmit to the $5d^1$ state. The energy transfer of the $Gd^{3+} \rightarrow Eu^{3+}$ and $Gd^{3+} \rightarrow Tb^{3+}$ may happen owing to that the $^5D_{3,4}$ (Tb^{3+}) and the $^5D_{0,1}$ (Eu^{3+}) states in the energy diagram lies lower than the ^6P_J state of Gd^{3+} [50–52]. On the other hand, the electrons of the ^7F_J ground state of Tb^{3+} via absorbing the energy can transmit to the $^5D_3$ excited state. Owing to the $^5D_1$ emission state of Eu^{3+} is lower than the $^5D_3$ state of Tb^{3+} [15]; thus the energy transfer of $Gd^{3+} \rightarrow Tb^{3+} \rightarrow Eu^{3+}$ may also occur in the $(Gd_{0.98-x}Tb_{0.02}Eu_x)_2O_3$ phosphors. Then the electrons of Tb^{3+} and Eu^{3+} relaxed from $^5D_3$ and $^5D_1$ to the $^5D_4$ and $^5D_0$, respectively. Back-jumping electrons of Tb^{3+} and Eu^{3+} from $^5D_4$ and $^5D_0$ excited state to

Figure 7 Illustration of the energy transfer processes for the $(Gd_{0.98-x}Tb_{0.02}Eu_x)_2O_3$ phosphors.

the $^7F_5$ ($^5D_4 \rightarrow {}^7F_5$ transition of Tb^{3+}) and $^7F_2$ ($^5D_0 \rightarrow {}^7F_2$ transition of Eu^{3+}) levels, respectively, and finally emit the green (547 nm) and red (613 nm) lights.

The PLE/PL thermal properties of phosphors are the important technological factors for applying in LEDs. Therefore, the PLE/PL emission spectra with the change of temperatures at the range of 298–523 K have been obtained to investigate the influence of temperature on the luminescence properties, and the activation energy of thermal quenching can be determined, which are shown in Fig. 8. The temperature variation does not bring about any appreciable change to the peak shape and positions of PLE (Fig. 8a, b) and PL (Fig. 8c) bands, but the emission intensities of Tb^{3+} and Eu^{3+} in $(Gd_{0.98-x}Tb_{0.02}Eu_x)_2O_3$ descend monotonically with the temperature increasing. Owing to the temperature has influence on the energy transfer, thus the declined rates are different. The reason for the emission intensity decreasing is generally due to the thermal quenching which was caused by the thermal activation of the intersecting point between the ground and the excited states [53]. The emission intensities of Tb^{3+} and Eu^{3+} at 323 K can retain $\sim$ 68.03 and $\sim$ 51.93% of their corresponding original values at 273 K, respectively. To further investigate the temperature-dependent thermal quenching phenomenon, the Arrhenius equation below has been utilized to assess the activation energy [54]:

$$\ln\left(\frac{I_0}{I} - 1\right) = \ln A - \frac{E_a}{kT} \tag{8}$$

where the E_a and T represent the objective activation energy and temperature (K), respectively. The A is a constant and the k is the Boltzmann constant (8.626×10^{-5} eV). The I_0 is the integrated emission intensity at room temperature, and the I is the integrated emission intensity at differently operated temperatures. Figure 8d shows the relationship between the $\ln[(I_0/I) - 1]$ and $1/kT$ for the thermal quenching of the $(Gd_{0.98-x}Tb_{0.02}Eu_x)_2O_3$ phosphors. As can be seen that the slope of the best fitting line is $- 0.2397$, so that the activation energy E_a is $\sim$ 0.2397 eV. The relatively high activation energy achieved in this work indicates that it possesses good thermal stability and it is an excellent candidate for application in LEDs.

As mentioned above, the relative I_{613}/I_{545} intensity ratio changed with the Eu^{3+} addition, thus the
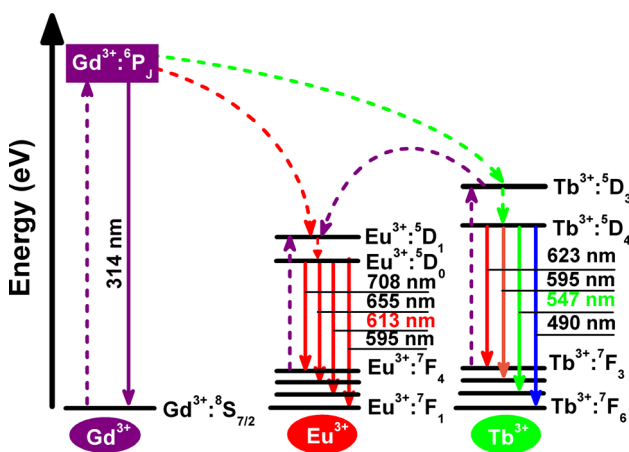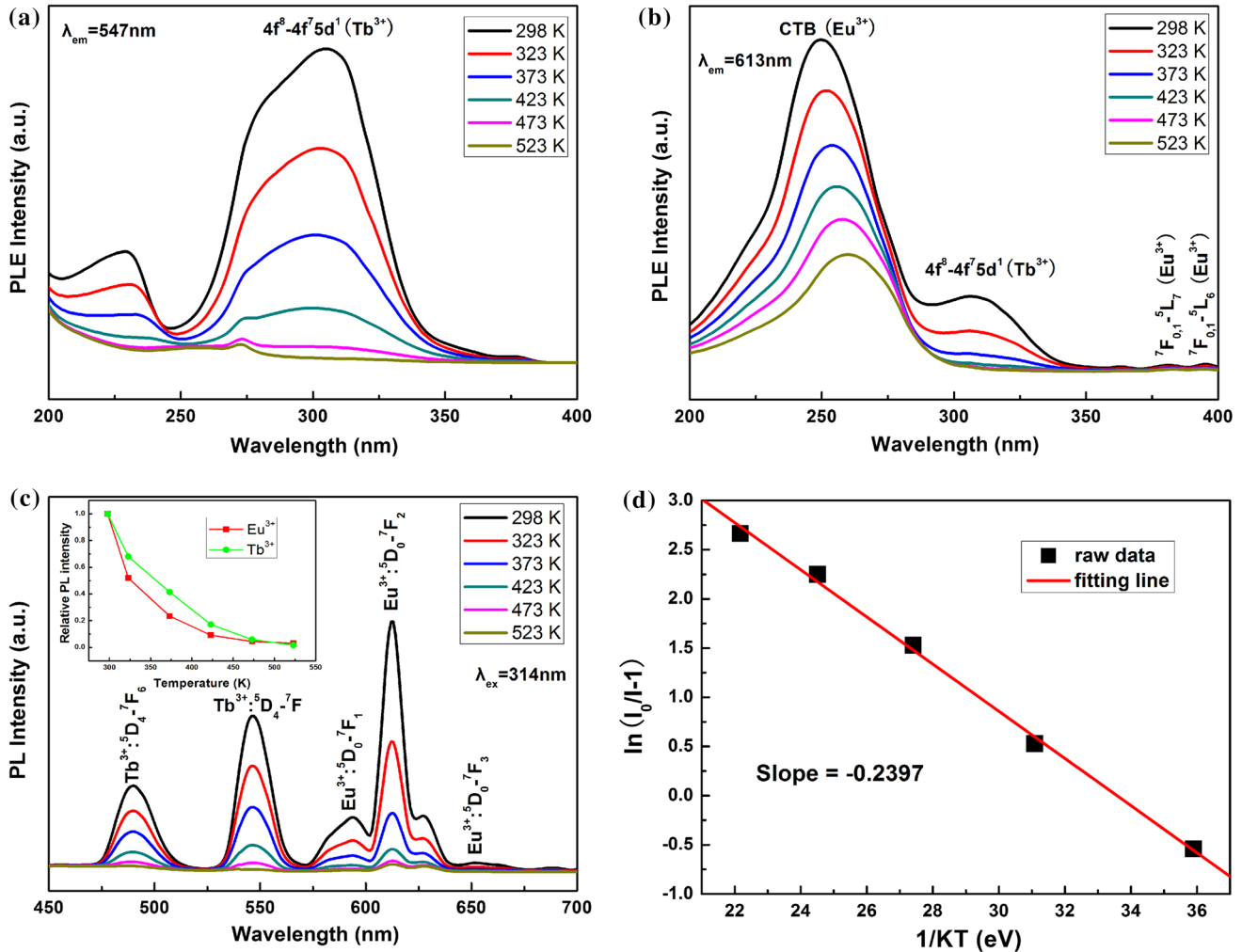
Figure 8 Dependence of the PLE (**a**, **b**) and PL (**c**) spectra of $(Gd_{0.96}Tb_{0.02}Eu_{0.02})_2O_3$ phosphors on the temperature; **d** linear relationship of the $\ln[(I_0/I) - 1]$ versus $1/kT$ activation energy graph for thermal quenching of the $(Gd_{0.96}Tb_{0.02}Eu_{0.02})_2O_3$ sample. The inset in **c** is the relative intensity of the 547 nm (Tb^{3+}) and 613 nm (Eu^{3+}) emissions as a function of the Eu^{3+} content.

emission color could be tuned via changing the relative Tb^{3+}/Eu^{3+} content, and this can be verified by the CIE chromaticity coordinates analysis. The CIE chromaticity coordinates for the emission of $(Gd_{0.98-x}Tb_{0.02}Eu_x)_2O_3$ (x = 0-0.05) under 314 nm excitation are shown in Fig. 9a. The samples with different Eu^{3+} content (the x value) were calculated to have the color coordinates (x, y) of (0.33, 0.56), (0.36, 0.55), (0.41, 0.50), (0.46, 0.46), (0.51, 0.42), (0.54, 0.39), and (0.54, 0.37) for the x = 0, 0.001, 0.005, 0.01, 0.02, 0.03, and 0.05, respectively, roughly corresponding to the green, yellowish-green, yellow, deep yellow, yellowish-orange, orange-red, and red colors, respectively. The corresponding color temperature can be calculated using the following formulas [55]:

$$T = -437n^3 + 3601n^2 - 6861n + 5514.31 \qquad (9)$$

and

$$n = (x - 0.332)/(y - 0.1858) \qquad (10)$$

The samples of the color temperature were ~ 5549 K (x = 0), ~ 5042 K (x = 0.001), ~ 4130 K (x = 0.005), ~ 3217 K (x = 0.01), ~ 2375 K (x = 0.02), ~ 1940 K (x = 0.03), and ~ 1834 K (x = 0.05). Figure 9b shows the vivid luminescence colors of the $(Gd_{0.98-x}Tb_{0.02}Eu_x)_2O_3$ phosphors with different Eu^{3+} contents under 254 nm UV excitation from a hand-held UV lamp. It is clearly observed that the emission color moves from green to yellow and eventually red regions, indicating that the color-tunable
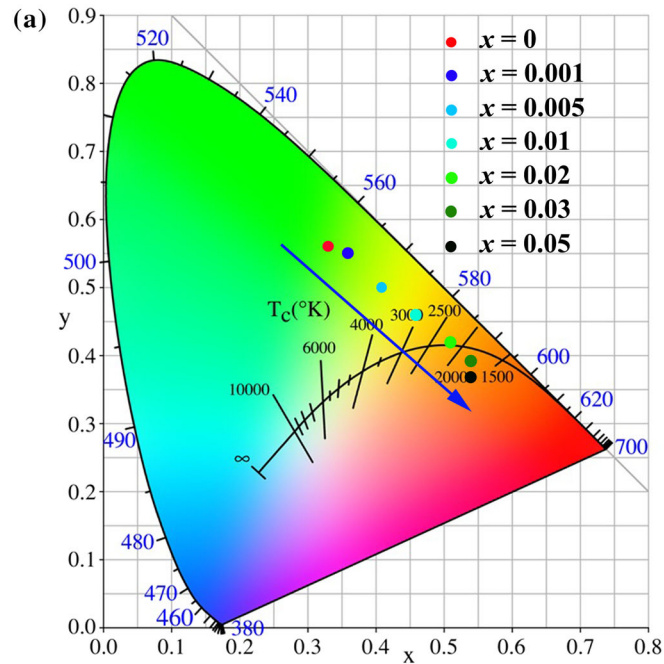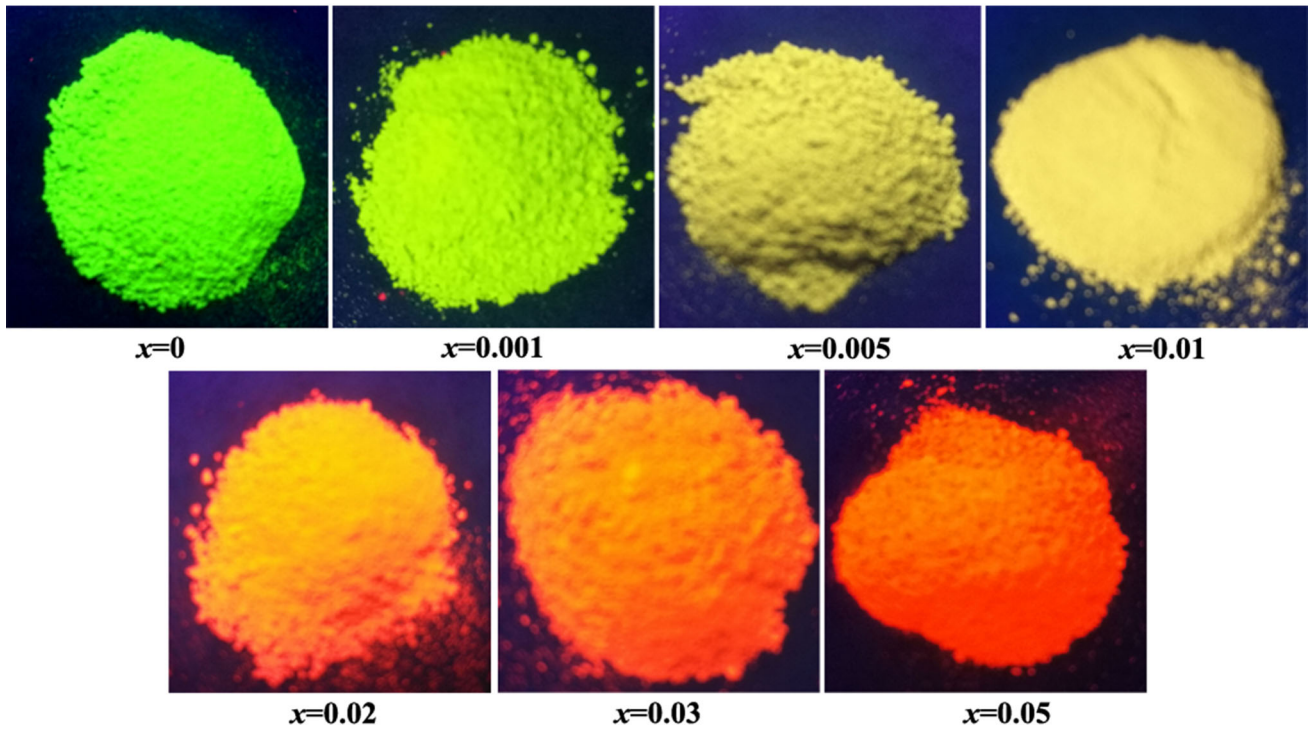
Figure 9 CIE chromaticity diagram for the emission of $(Gd_{0.98-x-}Tb_{0.02}Eu_x)_2O_3$ phosphors under 314 nm excitation (**a**). **b** is the appearances of luminescence for the $x = 0$, 0.001, 0.005, 0.01, 0.02, 0.03 and 0.05 samples under 254 nm excitation from a handheld UV lamp.

photoluminescence can be achieved though varying the Eu content (the x value).

In order to study the particle size and morphology effects on the luminescent properties of phosphors,

the $(Gd_{0.96}Tb_{0.02}Eu_{0.02})_2O_3$ phosphor with different morphologies and particle sizes as an example has been successfully obtained in present work. The effect of EG addition y ($y = 0$–0.5) on the particle sizes

and morphologies of the $(Gd_{0.96}Tb_{0.02}Eu_{0.02})_2O_3$ precursors has been studied using FE-SEM analysis (Supporting Information Figure S4). The morphologies of $(Gd_{0.96}Tb_{0.02}Eu_{0.02})_2O_3$ precursors with EG content increasing from $y = 0$ (pure water) to $y = 0.2$ are spherical with good dispersion, and the average particle size of the precursors steadily decreases (Fig. S4a: φ_a: $\sim$ 300 nm, Fig. S4b: φ_b: $\sim$ 240 nm and Fig. S4c: φ_c: $\sim$ 200 nm). The particle sizes of the precursors decrease with EG content increasing which can be explained as follows:

The supersaturation S is inversely proportional to the solubility product K_{sp} in the process of chemical precipitation [31], and the K_{sp} is related to the solubility C_s. The C_s can be calculated though the given following formula [56, 57]:

$$C_s \approx \exp\left[-\frac{z^+z^-e^2}{4\pi\varepsilon_0\varepsilon_r kT(r^{z+} + r^{z-})}\right] \quad (11)$$

where the r^{z+} and r^{z-} are the ion radius of take charge of z^+, z^-, respectively, the ε_0 is the vacuum permittivity, the ε_r is the relative permittivity constant of solvent. The ε_r of the water (78.5) is larger than the EG (37.7) [40] leading to the smaller C_s, and thus the S increases. At the same time, the homogeneous nucleation rate (R_N) can be calculated by the following formula [58]:

$$R_N = A\exp\left(\frac{-16\pi\sigma_{SL}v^2}{3k^3T^3\ln^2 S}\right) \quad (12)$$

where the R_N is the number of nuclei formed per unit time per unit volume, the A is a pre-exponential constant typically ranging from 10^{25} to 10^{56}, the σ_{SL} is the surface tension at the liquid/solid interface, the v is the atomic volume of the solute, the k is the Boltzmann constant, and the T is the temperature. The interface energy of EG (48.4 N/m) is smaller than water (72.8 N/m) [40], leading to the smaller surface tension at the liquid/solid interface σ_{SL}. Meanwhile, the increase in EG contents leads to the increase in supersaturation S and the decrease in interfacial tension σ_{SL}, which will increase the nucleation density leading to the smaller particle size. The results show that the spherical particle size will decrease with the EG content increasing. However, the spherical nanoparticles will be self-assembled when the particle size decreases to a certain degree, which are shown in Figs. S4d–S4f (Supporting Information Figure S4). As shown in Fig. S4d, the flower plate morphology begins to appear when the

EG content achieves to 30 vol% ($y = 0.3$), and the spherical particles mix with flower plate particles existed in precursors. When the ratio of EG and DI water content increases up to $y = 0.5$ as shown in Fig. S4f (Supporting Information Figure S4), the precursors are completely changed into the flower shape structure by its self-assembled.

The FE-SEM images of the $(Gd_{0.96}Tb_{0.02}Eu_{0.02})_2O_3$ precursors calcined at 1000 °C with different EG content ($y = 0$–0.5) are shown in Fig. S5 (Supporting Information Figure S5). It can be seen that the resultant samples even calcined at 1000 °C still maintain the good dispersion and morphology of the precursors under the different EG contents.

The PLE (Fig. 10a under 547 nm emission and Fig. 10b under 613 nm emission) and PL (Fig. 10c) spectra of the $(Gd_{0.96}Tb_{0.02}Eu_{0.02})_2O_3$ phosphors with different particle sizes and morphologies have been performed. Figure 10 shows that using the EG as the reaction solvent does not alter the shapes and positions of the PLE and PL peaks, being the same to the PLE and PL bands marked in Figs. 4 and 5a. The intensities of the 613 and 547 nm emission for Eu^{3+} and Tb^{3+} with the change of EG content are shown in Fig. 10c inset. It can be seen that the emission intensities of Eu^{3+} and Tb^{3+} all steadily decrease with the EG content increasing from 0 to 20 vol% and then increase. The reason for that phenomenon is that the bigger specific surface of phosphor will result in the higher scattering of the light, and thus the deteriorated emission intensity was achieved [59–61].

The substantial differences for the PL intensity may be caused by the particle morphology or the defects or the combined effects of two [45, 62]. For excited electrons, the higher defects content can improve its probability of non-radiative transitions, leading to the PL quenching [62]. On the other hand, the particle morphology can influence the PL intensity through the affecting the scattering degree of light produced and the packing density of phosphor crystals [45, 62]. In order to differentiate the two influencing factors, the decay curves of the 547 nm ($^5D_4 \rightarrow {}^7F_5$ transition of Tb^{3+}) and 613 nm ($^5D_0 \rightarrow {}^7F_2$ transition of Eu^{3+}) emission for the phosphors have been studied. Figures 11a and 11b show the luminescence decay curves of the $(Gd_{0.96}Tb_{0.02}Eu_{0.02})_2O_3$ (10 vol% EG) phosphor for the Tb^{3+} and Eu^{3+} emissions, respectively. The curves can be fitted with the single exponential decay by formula (4). The fitting results for the Tb^{3+} and Eu^{3+} emissions are shown in Fig. 11
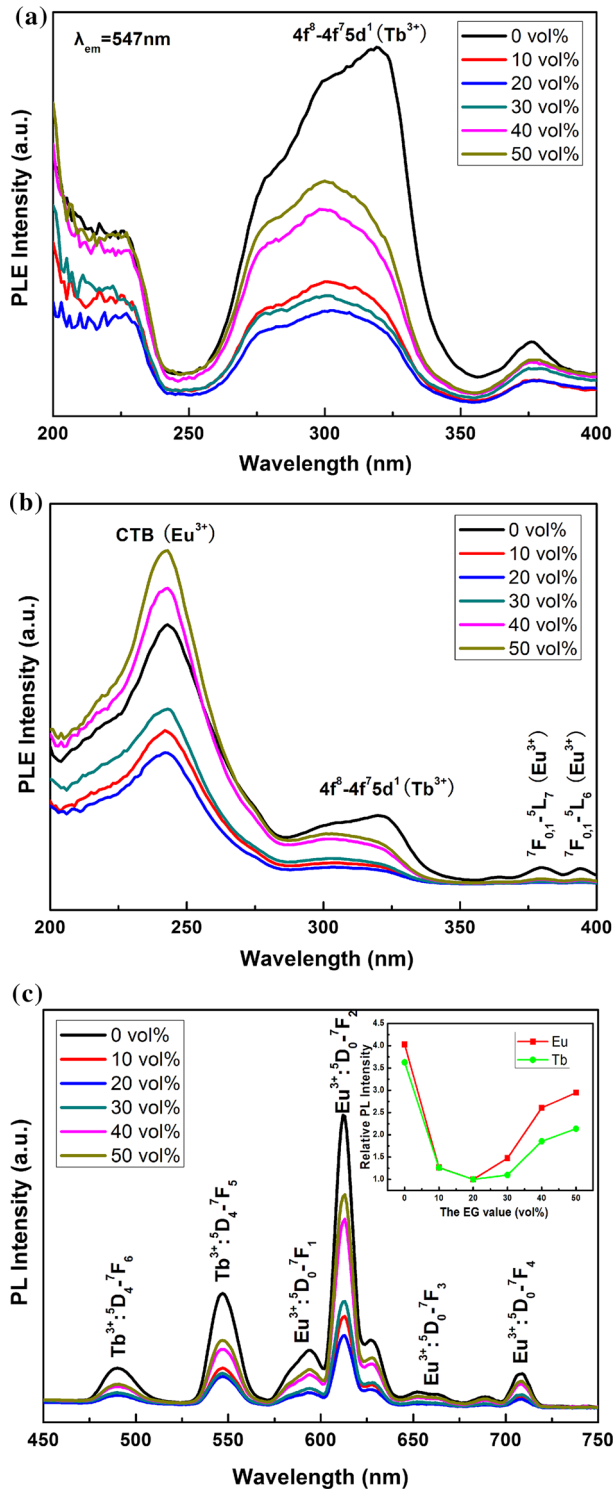
Figure 10 PLE (**a**, **b**) and PL (**c**) spectrum of $(Gd_{0.96}Tb_{0.02}$-$Eu_{0.02})_2O_3$ phosphors with different EG content (0–50 vol%), the PLE spectrum was obtained by monitoring the 547 nm (**a**) and 613 nm (**b**) emission, while the PL spectrum was obtained under UV excitation at 314 nm. Inset in **c** is the relative intensity of the 613 nm (Eu^{3+}) emission as a function of the EG content.
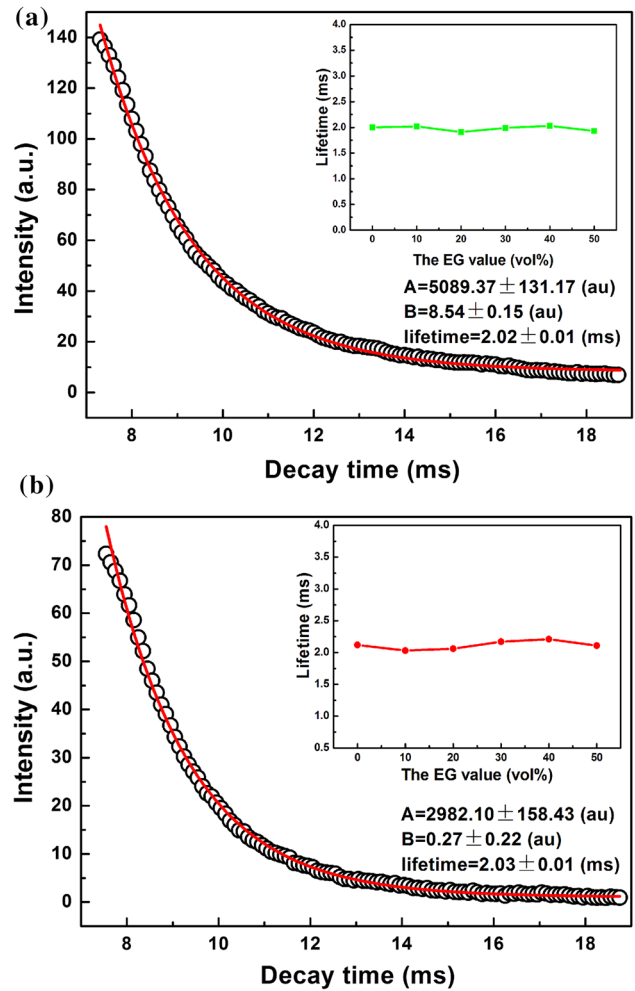

Figure 11 Fluorescence decay curves for the 547 nm (**a**) and 613 nm (**b**) emission of the $(Gd_{0.96}Tb_{0.02}Eu_{0.02})_2O_3$ phosphors. The embedded graph is the fluorescence lifetime of the different EG content ($y = 0$–0.5).

with $\tau_R = 2.02 \pm 0.01$ (ms), $A = 5089.37 \pm 131.17$ (a.u.), $B = 8.54 \pm 0.15$ (a.u.) and $\tau_R = 2.03 \pm 0.01$ (ms), $A = 2982.10 \pm 158.43$ (a.u.), $B = 0.27 \pm 0.22$ (a.u.), respectively. Further observation is that the fluorescence lifetimes have little changes with the EG content (0–50 vol%) changing (the insets of Fig. 11a, b), and all the samples have the similar lifetimes ($Tb^{3+} \sim 1.99 \pm 0.05$ ms and $Eu^{3+} \sim 2.07 \pm 0.05$ ms). The results may show that there is no significant difference in the defect concentration between these samples, since the more defect states will lead to non-radiative relaxation rates increasing, which will shorten the lifetimes of Eu^{3+} emission [62]. Thus, it can be concluded that the significant difference in emission intensities of 613 and 547 nm heavily depends on the morphology of the particles. The

average size of spherical particles gradually decreases with the EG content increasing from 0 to 20 vol%. Thus, the specific surface area of the particles is increased leading to the higher scattering of the light and the lower emission intensity. In addition, the agglomeration of small size particles may be the reason for the decrease in emission intensity. However, the average size of spherical particles gradually increases with the EG content continually increasing to the 50 vol%, resulting in the smaller scattering of the light, and thus improves the luminescence emission intensity [45, 62].

Conclusions

Color-tunable $(Gd_{0.98-x}Tb_{0.02}Eu_x)_2O_3$ ($x = 0$–.05) phosphors have been successfully obtained using the urea-based homogeneous precipitation method in the present work. Detailed characterizations by the combined techniques of XRD, XPS, ICP-OES, FE-SEM, HR-TEM, PLE/PL spectra and decay analysis have yielded the following main conclusions:

1. Growth of the particles is surface-diffusion related and follows the cubic-root law. Final sizes of the resultant particles are inversely proportional to nucleation density. Both the precursors and resultants of the $(Gd_{0.98-x}Tb_{0.02}Eu_x)_2O_3$ particles using the pure water as the solvent exhibit good dispersion and spherical morphology. Size-controlled and particle morphology changing from spheres to flower plate can be achieved via the EG addition owing to its lower permittivity constant and interface energy;

2. Under the UV excitation wavelength of 314 nm ($4f^8 \rightarrow 4f^7 5d^1$ transition of Tb^{3+}), the phosphors display the typical Tb^{3+} and Eu^{3+} emissions together, with the green emission at 547 nm ($^5D_4 \rightarrow {}^7F_5$ transition of Tb^{3+}) and red emission at 613 nm ($^5D_0 \rightarrow {}^7F_2$ transition of Eu^{3+}) being dominant. The Tb^{3+} and Eu^{3+} emissions vary significantly with the Eu^{3+} incorporation, and the emission color can thus be readily tuned from approximately green to red via adjusting the Eu^{3+} content. The quenching concentration is determined to be 2.0 at.% ($x = 0.02$) which is ascribed to the exchange between Eu^{3+} ions;

3. $Tb^{3+} \rightarrow Eu^{3+}$ energy transfer can be demonstrated by the two aspects: (a) the presence of Tb^{3+} excitation bands on the PLE spectra monitoring the Eu^{3+} emission; (b) the lifetime values for Tb^{3+} emission decreased with Eu^{3+} addition. The $Gd^{3+} \rightarrow Eu^{3+}$ and $Gd^{3+} \rightarrow Tb^{3+}$ energy transfers are also existed in the $(Gd_{0.98-x}Tb_{0.02-}Eu_x)_2O_3$ system. The efficiency of $Tb^{3+} \rightarrow Eu^{3+}$ energy transfer is calculated to be increased from 7.62 to 43.74% with the Eu^{3+} content (the x value) increasing from $x = 0.001$ to $x = 0.05$, respectively. The activation energy (E_a) is determined to be ~ 0.2397 eV through temperature-dependent analysis, indicating its good thermal stability;

4. The particle morphology/size does not alter the fluorescence lifetime, color coordinate, and color temperature, but brings about appreciable change to the emission intensity. Owing to the scattering of the light, the emission intensity firstly decreases and then improves with the EG addition which can be confirmed by the phosphor morphology of "spherical → spherical/flower shape → flower shape" variation.

Acknowledgements

Electronic supplementary material: The online version of this article (https://doi.org/10.1007/s10853-018-2505-z) contains supplementary material, which is available to authorized users.

References

[1] Sobral GA, Gomes MA, Avila JFM, Rodrigues JJ Jr, Macedo ZS, Hickmann JM, Alencar MARC (2016) Tailoring red-

green-blue emission from Er^{3+}, Eu^{3+} and Tb^{3+} doped Y_2O_3 nanocrystals produced via PVA-assisted sol-gel route. J Phys Chem Solids 98:81–89

[2] Selvalakshmi T, Sellaiyan S, Uedono A, Bose AC (2014) Investigation of defect related photoluminescence property of multicolour emitting Gd_2O_3:Dy^{3+} phosphor. RSC Adv 4:34257–34266

[3] Kumar JBP, Ramgopal G, Vidya YS, Anantharaju KS, Prasad BD, Sharma SC, Prashantha SC, Nagaswarupa HP, Kavyashree D, Nagabhushana H (2015) Green synthesis of Y_2O_3:Dy^{3+} nanophosphor with enhanced photocatalytic activity. Spectrochim Acta Pt A Mol Biol 149:687–697

[4] Bedekar V, Dutta DP, Mohapatra M, Godbole SV, Ghildiyal R, Tyagi AK (2009) Rare-earth doped gadolinia based phosphors for potential multicolor and white light emitting deep UV LEDs. Nanotechnology 20:125707

[5] Fulmek P, Nicolics J, Nemitz W, Wenzl FP (2017) On the impact of the temperature dependency of the phosphor quantum efficiency on correlated color temperature stability in phosphor converted LEDs. Mater Chem Phys 196:82–91

[6] Iqbal F, Kim S, Kim H (2017) Degradation of phosphor-in-glass encapsulants with various phosphor types for high power LEDs. Opt Mater 72:323–329

[7] Meza O, Villabona E, Diaz-Torres LA, Desirena H, Lopez JLR, Perez E (2014) Luminescence concentration quenching mechanism in Gd_2O_3:Eu^{3+}. J Phys Chem A 118:1390–1396

[8] Thongtem T, Phuruangrat A, Ham DJ, Lee JS, Thongtem S (2010) Controlled Gd_2O_3 nanorods and nanotubes by the annealing of $Gd(OH)_3$ nanorod and nanotube precursors and self-templates produced by a microwave-assisted hydrothermal process. CrystEngComm 12:2962–2966

[9] Seo S, Yang H, Holloway PH (2009) Controlled shape growth of Eu- or Tb-doped luminescent Gd_2O_3 colloidal nanocrystals. J Colloid Interface Sci 331:236–242

[10] Kim WJ, Gwag JS, Kang JG, Sohn Y (2014) Photoluminescence imaging of Eu(III), Eu(III)/Ag, Eu(III)/Tb(III), and Eu(III)/Tb(III)/Ag-doped $Gd(OH)_3$ and Gd_2O_3 nanorods. Ceram Int 40:12035–12044

[11] Li F, Liu H, Wei S, Suni W, Yu L (2013) Photoluminescent properties of Eu^{3+} and Tb^{3+} codoped Gd_2O_3 nanowires and bulk materials. J Rare Earth 31:1063–1068

[12] Yang L, Zhou LQ, Huang Y, Tang ZW (2011) Controlled synthesis of different morphologies of Gd_2O_3:Eu^{3+} crystals and shape-dependent luminescence properties. Mater Chem Phys 131:477–484

[13] Raleaooa PV, Roodt A, Mhlongo GG, Motaung DE, Ntwaeaborw OM (2018) Analysis of the structure, particle morphology and photoluminescent properties of ZnS:Mn^{2+} nanoparticulate phosphors. Optik 153:31–42

[14] Ding W, Liang P, Liu ZH (2017) Luminescence properties in relation to controllable morphologies of the $InBO_3$:Eu^{3+} phosphor. Mater Res Bull 94:31–37

[15] Li JG, Li X, Sun X, Ishigaki T (2008) Monodispersed colloidal spheres for uniform Y_2O_3:Eu^{3+} red-phosphor particles and greatly enhanced luminescence by simultaneous Gd^{3+} doping. J Phys Chem C 112:11707–11716

[16] Park IY, Kima D, Lee J, Lee SH, Kim KJ (2007) Effects of urea concentration and reaction temperature on morphology of gadolinium compounds prepared by homogeneous precipitation. Mater Chem Phys 106:149–157

[17] Teng X, Li J, Duan G, Liu Z (2016) Development of Tb^{3+} activated gadolinium aluminate garnet ($Gd_3Al_5O_{12}$) as highly efficient green-emitting phosphors. J Lumin 179:165–170

[18] Zhang JW, Zhu PL, Li JH, Chen JM, Wu ZH, Zhang ZJ (2009) Fabrication of octahedral-shaped polyol-based zinc alkoxide particles and their conversion to octahedral polycrystalline ZnO or single-crystal ZnO nanoparticles. Cryst Growth Des 9:2329–2334

[19] Dai SH, Liu YF, Lu YN, Min HH (2010) Microwave solvothermal synthesis of Eu^{3+}-doped (Y, Gd)$_2O_3$ microsheets. Powder Technol 202:178–184

[20] Teng X, Wang W, Cao Z, Li J, Duan G, Liu Z (2017) The development of new phosphors of Tb^{3+}/Eu^{3+} co-doped $Gd_3Al_5O_{12}$ with tunable emission. Opt Mater 69:175–180

[21] Mukhergee ST, Sudarsan V, Sastry PU, Patra AK, Tyagi AK (2012) Annealing effects on the microstructure of combustion synthesized Eu^{3+} and Tb^{3+} doped Y_2O_3 nanoparticles. J Alloys Compd 519:9–14

[22] Yang J, Li CX, Quan ZW, Zhang CM, Yang PP, Li YY, Yu CC, Lin J (2008) Self-assembled 3D flowerlike Lu_2O_3 and Lu_2O_3:Ln^{3+} (Ln = Eu, Tb, Dy, Pr, Sm, Er, Ho, Tm) microarchitectures: ethylene glycol-mediated hydrothermal synthesis and luminescent properties. J Phys Chem C 112:12777–12785

[23] Li J, Li JG, Zhang Z, Wu X, Liu S, Li X, Sun X, Sakka Y (2012) Effective lattice stabilization of gadolinium aluminate garnet (GdAG) via Lu^{3+} doping and development of highly efficient (Gd,Lu)AG:Eu^{3+} red phosphors. Sci Technol Adv Mater 13:035007

[24] Li JG, Li JK, Zhu Q, Wang X, Li X, Sun X, Sakka Y (2015) Photoluminescent and cathodoluminescent performances of Tb^{3+} in Lu^{3+}-stabilized gadolinium aluminate garnet solid-solutions of $[(Gd_{1-x}Lu_x)_{1-y}Tb_y]_3Al_5O_{12}$. RSC Adv 5:59686–59695

[25] Li S, Guo N, Liang Q, Ding Y, Zhou H, Ouyang R, Lü W (2018) Energy transfer and color tunable emission in Tb^{3+}, Eu^{3+} co-doped $Sr_3LaNa(PO_4)_3F$ phosphors. Spectrochim Acta A 190:246–252

[26] Li B, Huang X, Guo H, Zeng Y (2018) Energy transfer and tunable photoluminescence of LaBWO6:Tb$_{3+}$, Eu$_{3+}$ phosphors for near-UV white LEDs. Dyes Pigments 150:67–72

[27] Gopi S, Jose SK, Sreeja E, Manasa P, Unnikrishnan NV, Joseph C, Biju PR (2017) Tunable green to red emission via Tb sensitized energy transfer in Tb/Eu codoped alkali fluoroborate glass. J Lumin 192:1288–1294

[28] Chen Y, Zhang K, Wang H, Ren X, Wang X (2017) Tunable light emission of amorphous Eu^{3+}/Tb^{3+} co-doped MgAl-hydroxide salts depending on phase transition. J Non-Cryst Solids 478:41–49

[29] Allred AL (1961) Electronegativity values from thermochemical date. J Inorg Nucl Chem 17:215–221

[30] Li J, Teng X, Wang W, Zhao W, Liu Z (2017) Investigation on the preparation and luminescence property of (Gd$_{1−x}$-Dy$_x$)$_2$O$_3$ ($x = 001–010$) spherical phosphors. Ceram Int 43:10166–10173

[31] Cushing BL, Kolesnichenko VL, O'Connor CJ (2004) Recent advances in the liquid-phase syntheses of inorganic nanoparticles. Chem Rev 104:3893–3946

[32] Wang W, Li J, Duan G, Zhao W, Cao B, Liu Z (2017) Morphology/size effect on the luminescence properties of the [(Y$_x$Gd$_{1−x}$)$_{098}$Dy$_{002}$]$_2$O$_3$ phosphor with enhanced yellow emission. J Lumin 192:1056–1064

[33] Lamer VK, Dinegar RH (1950) Theory, production and formation of monodispersed hydrosols. J Am Chem Soc 72:2494

[34] Li J, Li JG, Li X, Sun X (2016) Tb^{3+}/Eu^{3+} codoping of Lu^{3+}-stabilized Gd$_3$Al$_5$O$_{12}$ for tunable photoluminescence via efficient energy transfer. J Alloys Compd 670:161–169

[35] Kang JG, Jung Y, Min BK, Sohn Y (2014) Full characterization of Eu(OH)$_3$ and Eu$_2$O$_3$ nanorods. Appl Surf Sci 314:158–165

[36] Kang JG, Min BK, Sohn Y (2015) Synthesis and characterization of Gd(OH)$_3$ and Gd$_2$O$_3$ nanorods. Ceram Int 41:1243–1248

[37] Arul NS, Mangalaraj D, Kim TW (2015) Photocatalytic degradation mechanisms of CeO$_2$/Tb$_2$O$_3$ nanotubes. Appl Surf Sci 349:459–464

[38] Qu D, Xie F, Meng H, Gong L, Zhang W, Chen J, Li G, Liu P, Tong Y (2010) Preparation and characterization of nanocrystalline CeO$_2$–Tb$_2$O$_3$ films obtained by electrochemical deposition method. J Phys Chem C 114:1424–1429

[39] Luo N, Yang C, Tian X, Xiao J, Liu J, Chen F, Zhang D, Xu D, Zhang Y, Yang G, Chen D, Li L (2014) A general top-down approach to synthesize rare earth doped-Gd$_2$O$_3$ nanocrystals as dualmodal contrast agents. J Mater Chem B 2(35):5891–5897

[40] Li JG, Zhu Q, Li X, Sun X, Sakka Y (2011) Colloidal processing of Gd$_2$O$_3$:Eu^{3+} red phosphor monospheres of tunable sizes: solvent effects on precipitation kinetics and photoluminescence properties of the oxides. Acta Mater 59:3688–3696

[41] Som S, Das S, Dutta S, Visser HG, Pandey MK, Kumar P, Dubeye RK, Sharma SK (2015) Synthesis of strong red emitting Y$_2$O$_3$:Eu^{3+} phosphor by potential chemical routes: comparative investigations on the structural evolutions, photometric properties and Judd-Ofelt analysis. RSC Adv 5:70887–70898

[42] Wang ZJ, Wang P, Zhong JP, Liang HB, Wang J (2014) Phase transformation and spectroscopic adjustment of Gd$_2$O$_3$:Eu^{3+} synthesized by hydrothermal method. J Lumin 152:172–175

[43] Li J, Li JG, Zhang Z, Wu X, Liu S, Li X, Sun X, Sakka Y (2012) Gadolinium aluminate garnet (Gd$_3$Al$_5$O$_{12}$): crystal structure stabilization via lutetium doping and properties of the (Gd$_{1−x}$Lu$_x$)$_3$Al$_5$O$_{12}$ solid solutions (x = 0–0.5). J Am Ceram Soc 95(5):931–936

[44] Zhu Q, Li JG, Li X, Sun X (2010) Selective processing, structural characterization, and photoluminescence behaviors of single crystalline (Gd$_{1−x}$Eu$_x$)$_2$O$_3$ nanorods and nanotubes. Curr Nanosci 6(5):496–504

[45] Dai Q, Song H, Wang M, Bai X, Dong B, Qin R, Qu X, Zhang H (2008) Size and concentration effects on the photoluminescence of La$_2$O$_2$S:Eu^{3+} nanocrystals. J Phys Chem C 112:19399–19404

[46] Blasse G (1968) Energy transfer in oxidic phosphors. Phys Lett A 28:444–445

[47] Dexter DL (1953) A theory of sensitized luminescence in solids. J Chem Phys 21:836–850

[48] Reisfeld R, Greenberg E, Velapoldi R, Barnett B (1972) Luminescence quantum efficiency of Gd and Tb in borate glasses and the mechanism of ET between them. J Chem Phys 56:1698–1705

[49] Dexter DL, Schulman JH (1954) Theory of concentration quenching in inorganic phosphors. J Chem Phys 22:1063–1070

[50] Dieke GH, Crosswhite HM (1963) The spectra of the doubly and triply ionized rare earth. Appl Opt 2:675–686

[51] Wegh RT, Meijerink A, Lamminmaki RJ, Holsa J (2000) Extending dieke's diagram. J Lumin 87–89:1002–1004

[52] Peijzel PS, Meijerink A, Wegh RT, Reid MF, Burdick GW (2005) A complete 4fn energy level diagram for all trivalent lanthanide ions. J Solid State Chem 178:448–453

[53] Hertle E, Chepyga L, Batentschuk M, Zigan L (2017) Influence of codoping on the luminescence properties of YAG:Dy for high temperature phosphor thermometry. J Lumin 182:200–207

[54] Zheng JH, Cheng QJ, Wu SQ, Guo ZQ, Zhuang YX, Lu YJ, Li Y, Chen C (2015) An efficient blue-emitting

$Sr_5(PO_4)_3Cl:Eu^{2+}$ phosphor for application in near-UV white light-emitting diodes. J Mater Chem C 3:11219–11227

[55] Mccamy CS (1992) Correlated color temperature as an explicit function of chromaticity coordinates. Color Res Appl 17:142–144

[56] Chen HI, Chang HY (2004) Homogeneous precipitation of cerium dioxide nanoparticles in alcohol/water mixed solvents. Colloid Surf A 242(1–3):61–69

[57] Yoo HS, Jang HS, Im WB, Kang JH, Jeon DY (2007) Particle size control of a monodisperse spherical $Y_2O_3:Eu^{3+}$ phosphor and its photoluminescence properties. J Mater Res 22(7):2017–2024

[58] Li JG, Li X, Sun X, Ikegami T, Ishigaki T (2008) Uniform colloidal spheres for $(Y_{1-x}Gd_x)_2O_3$ ($x = 0$–1): formation mechanism, compositional impacts, and physicochemical properties of the oxides. Chem Mater 20:2274–2281

[59] Jing X, Ireland T, Gibbons C, Barber DJ, Silver J, Vecht A (1999) Control of $Y_2O_3:Eu$ spherical particle phosphor size, assembly properties, and performance for FED and HDTV. J Electrochem Soc 146:4654–4658

[60] Yoo JS, Lee JD (1997) The effects of particle size and surface recombination rate on the brightness of low-voltage phosphor. J Appl Phys 81:2810–2813

[61] Vila LDD, Stucchi EB, Davolos MR (1997) Preparation and characterization of uniform, spherical particles of Y_2O_2S and $Y_2O_2S:Eu$. J Mater Chem 7:2113–2116

[62] Song HW, Wang JW, Chen BJ, Peng HS, Lu SZ (2003) Size-dependent electronic transition rates in cubic nanocrystalline europium doped yttria. Chem Phys Lett 376:1–5